Available online at www.sciencedirect.com

ScienceDirect

Underground Space 22 (2025) 21–38

www.keaipublishing.com/undsp

Research Paper

Bleed-off control on post-injection seismicity in enhanced geothermal systems

Iman R. Kivi [a,*], Victor Vilarrasa [b], Kwang-Il Kim [c], Hwajung Yoo [d], Ki-Bok Min [d]

[a] Department of Earth Science and Engineering, Imperial College London, London SW72BP, UK
[b] Global Change Research Group, IMEDEA, CSIC-UIB, Esporles 07190, Spain
[c] Disposal Safety Evaluation Research Division, Korea Atomic Energy Research Institute, Daejeon 34057, Republic of Korea
[d] Department of Energy Systems Engineering and Research Institute of Energy and Resources, Seoul National University, Seoul 08826, Republic of Korea

Received 29 April 2024; received in revised form 18 July 2024; accepted 26 August 2024
Available online 18 December 2024

Abstract

Deep geothermal reservoirs could provide widespread access to clean and renewable energy around the world. However, hydraulic stimulation of these reservoirs to create sufficient injectivity and heat extraction has frequently induced earthquakes during and, in particular, after reservoir stimulation, which raises public concerns. This study aims to provide a possible explanation for post-injection seismicity and understand how it responds to well bleed-off as a common industrial practice to control such seismic activity. To this end, we perform coupled hydromechanical simulations of reservoir stimulation in a conceptual model comprising a deep granitic reservoir intersected by a network of long fractures and a nearby, critically-stressed fault. We find a combination of mechanisms triggering post-injection seismicity with time delays of several months after stopping injection: (1) poroelastic stressing that transmits normal and shear stress and causes undrained pressure buildup on the fault, (2) fracture-dominated pore pressure migration toward the fault, and (3) long-lasting along-the-fault pressure diffusion toward pre-stressed fault patches, promoted by dilation-induced fault permeability changes. In this setting, bleed-off causes rapid pressure decline in the near-wellbore region but marginal pressure changes farther away. The resulting attenuations of pore pressure and shear stress on the fault plane may not be enough to prevent fault reactivation. Bleed-off may counterintuitively accelerate fault slip by rapid relaxation of normal stress on the fault, which not only brings the stress state closer to failure conditions, but also accelerates pore pressure diffusion along the fault by slightly increasing its permeability. We show that bleed-off can effectively control post-injection seismicity only if rupture initiates from a structure in close proximity and with sufficient hydraulic connection to the wellbore. Future research should be directed toward the optimization of stimulation and post-stimulation design in light of the involved triggering mechanisms and through effective combination with subsurface characterization to control post-injection seismicity.

Keywords: Enhanced geothermal system; Stimulation-induced seismicity; Post-injection earthquake; Triggering mechanisms; Coupled multi-physics modeling

1 Introduction

Hydraulic stimulation techniques are broadly employed in enhanced geothermal systems (EGS) for creating conductive flow paths that ensure sufficient production of hot fluid from deep (4–6 km) crystalline rock of (ultra-) low permeability (Majer et al., 2007; Tomac & Sauter, 2018; Jia et al., 2022). These techniques involve injection of large fluid volumes at elevated pressures to create new fractures and/or cause the pre-existing ones to slip (McClure & Horne, 2011). Shearing-induced dilation along the rough fracture surfaces could permanently increase fracture permeability by several orders of magnitude (Rutqvist et al., 2015; Rinaldi & Rutqvist, 2019). However, this stimulation mechanism may bring about an unsolicited side-effect: the release of stored elastic energy in rock in a seismic way following an abrupt slip (Evans et al., 2012; Ji et al., 2022; De Simone et al., 2023). Although the major-

* Corresponding author.
E-mail address: i.rahimzadeh-kivi@imperial.ac.uk (I.R. Kivi).
Peer review under the responsibility of Tongji University

https://doi.org/10.1016/j.undsp.2024.08.009
2467-9674/© 2024 Tongji University. Publishing Services by Elsevier B.V. on behalf of KeAi Communications Co. Ltd.
This is an open access article under the CC BY-NC-ND license (http://creativecommons.org/licenses/by-nc-nd/4.0/).

Nomenclature

a	Hydraulic aperture in the embedded fracture model
a_i	Initial hydraulic aperture of the fracture
CFS	Coulomb failure stress
CODE_BRIGHT	COupled DEformation, BRIne, Gas and Heat Transport
D	Hydraulic diffusivity
E	Young's modulus
EGS	Enhanced geothermal system
k	Permeability
k_m	Permeability of the background fracture matrix
k_n	Normal stiffness
k_s	Shear stiffness
L	Length
L^*	Characteristic length of fractures for bleed-off effectiveness
M_w	Moment magnitude
M_L	Local magnitude
p	Pore pressure
s	Fracture spacing in the embedded fracture model
t	Time
TLS	Traffic light system
u_n	Normal displacement
u_s	Shear displacement
w	Thickness of the fracture in the embedded fracture model
α	Biot coefficient
ε_v	Volumetric strain
μ	Friction coefficient
ν	Poisson's ratio
ρ_b	Bulk density
σ_h	Horizontal stress
σ_l	Longitudinal stress
σ_n	Normal stress
σ_v	Vertical stress
σ'_n	Effective normal stress
τ	Shear stress
ϕ	Porosity

ity of stimulation-induced seismic events are in the form of microtremors, only detectable by sensitive seismic sensors, earthquakes large enough to be felt on the surface have occasionally occurred (Majer et al., 2007; Evans et al., 2012; Buijze et al., 2019; Schmittbuhl et al., 2021). Proper management of injection-induced seismicity is thus contemplated as an imperative step to build momentum behind future EGS projects (Gaucher et al., 2015; Kivi et al., 2023).

A felt earthquake may occur if a large portion of a fault reactivates (Zang et al., 2014). The fault reactivation could be explained by injection-induced perturbations in the state of effective stress, referred to as seismicity triggering mechanisms. A primary mechanism widely leveraged to explain fault reactivation is pore pressure diffusion (Healy et al., 1968; Shapiro et al., 1999; Mukuhira et al., 2017). The pore pressure increase diffusing away from the injection source into the surrounding rock mass—proportionally to the square root of time—could destabilize an intersecting fault by reducing the effective normal stress, clamping it. Nevertheless, induced seismicity may render much more complex spatiotemporal evolution patterns to be captured solely by the pore pressure diffusion concept (Segall & Lu, 2015; Vilarrasa et al., 2021; Ge & Saar, 2022). Significant challenges arise when explaining large earthquakes that unexpectedly nucleate beyond the stimulated rock volume and often—but not always—after stopping the injection. The damaging 2017 Pohang, South Korea, earthquake with moment magnitude M_w 5.5 (Kim et al., 2022) and the 2006 Basel, Switzerland, earthquake with local magnitude M_L 3.4 (Bachmann et al., 2011), alongside several sequences in a number of other EGS sites, e.g., Soultz-sous-Forêts in France (Evans et al., 2005) or Paralana in Australia (Albaric et al., 2014), reside in this category of seismicity trailing well shut-in. Yet, the causative mechanisms of the observed surge in post-injection seismic activities are less well understood.

Extensive research has been dedicated to the understanding of post-injection seismicity in geoenergy projects. Insights gained from modeling efforts and direct observations in the field and underground rock laboratories suggest that a combination of various physical processes should enable the development of more accurate explanations for post-injection seismicity (Hsieh & Bredehoeft, 1981; De Simone et al., 2017; Mukuhira et al., 2017; Kim et al., 2022; Ge & Saar, 2022; Sáez & Lecampion, 2023; Boyet et al., 2023; Kivi et al., 2024a). The proposed mechanisms include, among others, (1) delayed pore pressure diffusion, progressively enlarging the region affected by pressure perturbations, (2) static stress transfer by seismic and/or aseismic slip of a fault, and (3) poroelastic and (4) thermoelastic stressing driven by the porous rock deformation under constrained subsurface conditions in response to pressure and temperature changes, respectively. These physical processes are tightly coupled but operate at remarkably different spatial and temporal scales (Taron et al., 2009). While pore pressure diffusion and aseismic slip progress gradually, stress transfers of any origin take place instantaneously through the rock, affecting a large reservoir body. Furthermore, the presence of fractures frequently occurring at varying scales in the intrinsically brittle crystalline rock hosting EGS projects introduces significant nonlinearities and discontinuities in the thermo-hydromechanical response of the rock to fluid injection and, thus, the relative contribu-

tions of the seismicity triggering mechanisms (Zareidarmiyan et al., 2020; Kivi et al., 2024a). Accordingly, some mechanisms that inhibit slip along faults with certain attributes may gradually vanish after well shut-in, while some others with destabilizing effects may persist for days or even months and establish interactions with nearby faults or fault segments more prone to slip, altogether contributing to long-lived post-injection seismicity (Segall & Lu, 2015; De Simone et al., 2017). Efforts toward managing trailing seismicity need to take relevant mechanistic and structural complexities into account.

Extensive efforts have been dedicated to the development of seismicity forecasting models (McGarr, 2014; Zang et al., 2014; Alghannam & Juanes, 2020). Nevertheless, these models commonly fail to anticipate the observed counterintuitive surge in large-magnitude seismic events in the post-injection period because the input model variables, including the total injected fluid volume, injection rate and pressure, remain almost unchanged or rapidly decline with time after cessation of fluid injection. In the absence of a reliable seismicity prediction approach, industrial operators commonly respond to induced seismicity by devising the so-called traffic light system (TLS), a monitoring-based reactive framework regulated by a series of adaptive actions to implement whenever one or more indicators (usually event magnitude) exceed the pre-defined thresholds (Verdon & Bommer, 2021; De Simone et al., 2023). The TLS strategy has demonstrated varying degrees of success in the mitigation of co-injection seismicity by reducing or halting injection (Baisch et al., 2019). However, the capability to alleviate the rate and magnitude of post-injection seismicity is limited by partial loss of control over their management, exacerbating the risk and hazard these events may pose (Schultz et al., 2022). Indeed, possible mitigation measures would exclusively rely on well bleed-off, i.e., opening the wellhead to impose hydrostatic pressure conditions in the well. There are a few modeling studies that have found bleed-off effective in managing post-injection seismicity by restricting the spatial and temporal extents of reservoir exposure to elevated pore pressure (Karvounis & Wiemer, 2022). However, contradictory observations have been encountered at EGS sites elsewhere. For example, at the Pohang EGS site, bleed-off after a M_L 2.2 event during the second stimulation phase could successfully keep the seismicity rate at a stable level (Park et al., 2020), whereas it could not prevent the 2017 M_w 5.5 earthquake that took place during bleed-off of one of the two operating boreholes after the fifth stimulation phase (Kim et al., 2022). Whether and under which conditions bleed-off may succeed or fail remain open questions central to the effective management of trailing seismic sequences at EGS sites.

We here conduct coupled hydromechanical simulations of stimulation of a fractured reservoir to understand how post-injection seismicity could take place and be affected by two common-practice industrial protocols after stopping injection: well shut-in or bleed-off. We first explain the numerical model comprising a fracture network targeted for hydraulic stimulation and a nearby, major fault, embedded as equivalent porous media in a granitic reservoir. This semi-hypothetical model is constructed with a reference to the Pohang EGS site where a large fault was reactivated close to the injection wells (Kim et al., 2022). We consider two model settings: (1) the base-case scenario in which the fault is hydraulically isolated by the low-permeability rock matrix from the fracture network and (2) the case of the fracture network intersecting the fault. Next, we present the results for injection-induced evolutions of pore pressure and state of stress, propose a combination of mechanisms that explain post-injection seismicity and analyze how they are affected by well bleed-off or shut-in after stopping injection in each of the model settings. This study has significant implications for the optimization of the stimulation design and subsurface characterization to control post-injection seismicity.

2 Methods

2.1 Geometry

The model in this study represents a conceptual EGS project targeting a granitic reservoir at a depth of 4000 m (Fig. 1(a)). The vertical wellbore intersects a network of fractures with varying dip angles from 30° to 70°. Fractures, named f1 to f7, are 0.2-m thick and approximately 500-m long. We consider a 1000-m long, 70°-dipping fault with a thickness of 2 m, whose central point is located at a horizontal distance of 500 m from the wellbore. The fault and the tip of the nearby fracture f5 are spaced 11 m apart in our base-case model, where the low-permeability rock matrix prevents a direct hydraulic connection between the fault and the fracture network (Fig. 1(a)). This model geometry may arguably bear resemblance to the Pohang EGS site where fractures subject to cycles of hydraulic stimulation did not have a direct hydraulic connection to the main fault (Kim et al., 2022). We also consider another geometry that features the intersection of the fault and fracture f5 while all other parameters remain unchanged. In all models, we assume a plane-strain geometry with a length of 1800 m and a height of 1400 m. The geometry size, achieved through a number of trials, is extended enough on the sides to impose minimum boundary effects on the numerical results.

2.2 Material properties

The hydromechanical properties of the material forming the model are presented in Table 1. We assign typical properties of a granitic rock to the reservoir (Rutqvist et al., 2015; Kwon et al., 2019; Kivi et al., 2023). We assume constant reservoir rock properties with a low permeability of 10^{-18} m^2 and a high Young's modulus of 60 GPa. The fault and fractures are represented in our continuum numerical approach as equivalent porous media. The so-called continuum fracture model considers a uniform distribution of sub-parallel fractures with hydraulic aperture a and fixed

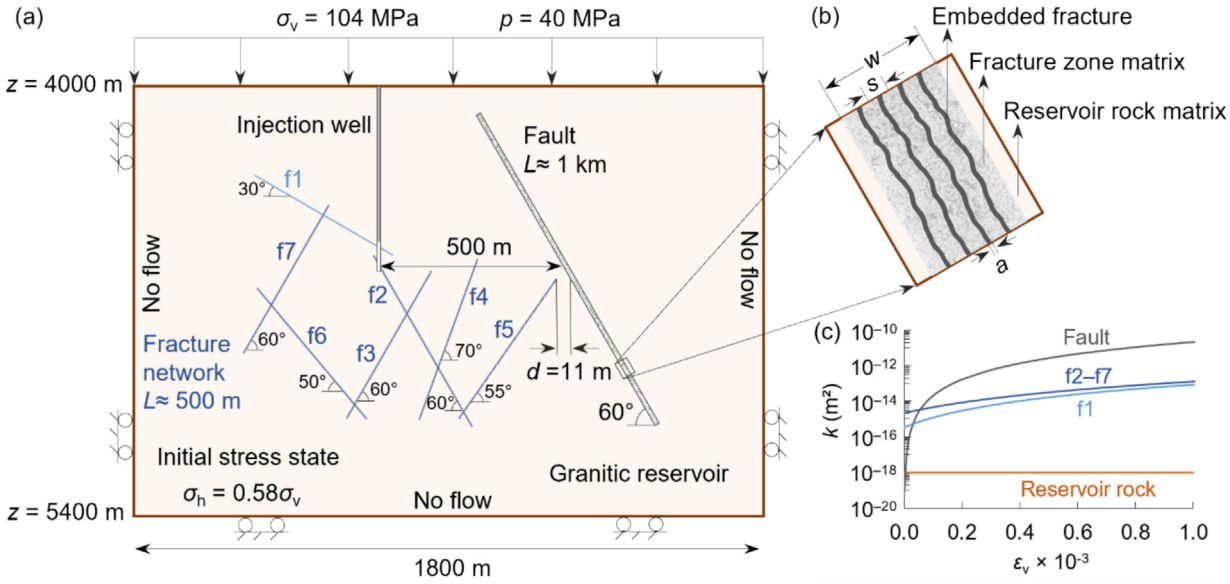

Fig. 1. Numerical model setup. (a) Base-case model geometry with no hydraulic connection between the fault and fracture network together with initial and boundary conditions, (b) embedded fracture model and associated parameters used for modeling hydromechanical behavior of fault and fractures, and (c) permeability as a function of volumetric strain for different constituents of the numerical model.

Table 1
Hydromechanical properties of rock materials included in the model.

Parameters		Reservoir rock	Fracture f1	Fractures f2–f7	Fault
General rock properties	Bulk density, ρ_b (kg/m^3)	2630	2630	2630	2630
	Porosity, ϕ	0.01	0.01	0.01	0.01
	Matrix permeability, k_m (m^2)	10^{-18}	10^{-19}	10^{-19}	10^{-19}
	Young's modulus, E (GPa)	60	6.67	6.67	1 or 40
	Poisson's ratio, ν	0.2	0.33	0.33	0.2
	Biot coefficient, α	0.45	1	1	1
Fracture and fault properties	Thickness, w (m)	–	0.2	0.2	2
	Fracture spacing, s (m)	–	0.025	0.025	0.5
	Initial hydraulic aperture, a_i (m)	–	4.7×10^{-6}	8.7×10^{-6}	10^{-7}
	Friction coefficient, μ	–	0.6	0.6	0.6

spacing s in a background low-permeability matrix of thickness w (Fig. 1(b)). The model parameters a and s can be adjusted in a way reproducing the real fracture transmissivity. Assuming that fluid flow within a fracture represented by parallel and smooth surfaces follows the cubic law (Witherspoon et al., 1980), the equivalent permeability of the continuum fracture medium, k, can be written as

$$k = k_m + \frac{a^3}{12s}, \tag{1}$$

where k_m is the permeability of the background fracture matrix.

Neglecting shearing-induced fracture dilation, the aperture at each time comprises two components: the initial aperture under in situ stress conditions, a_i, and elastic opening/closure as a result of changes in pore pressure and stress components, Δa. Assuming that the deformation is localized and takes place dominantly perpendicular to the embedded fractures, the average change in the hydraulic aperture can be approximated as a linear function of the volumetric strain, ε_v, resulting in (Olivella & Alonso, 2008)

$$a = a_i + \Delta a = a_i + s\varepsilon_v. \tag{2}$$

The initial hydraulic apertures and fracture spacings are set to return intrinsic permeability of 10^{-19} m^2 for the fault, 3.5×10^{-16} m^2 for fracture f1, and 2.2×10^{-15} m^2 for other fractures. The initial permeability of fracture f1 is nearly one order of magnitude smaller than that of other fractures due to its orientation relative to the maximum in situ principal stress, i.e., the overburden stress in our case. We use a relatively large spacing for the fault to reproduce a rapid permeability increase by orders of magnitude upon pressurization, a trend typical of tight geomaterials (Wibberley & Shimamoto, 2003; Hoseini et al., 2009; Rutqvist, 2012). In contrast, a small spacing value assigned to other fractures results in more gradual permeability variations, required to capture wellhead pressure changes representative of EGS stimulations.

Another set of parameters that need to be assigned is the equivalent elastic moduli for the continuum representations of the structural discontinuities. In a discontinuum representation of fractures, stiffness parameters establish the relationship between the applied stress and the corre-

sponding fracture deformation under the linear elastic assumption (Goodman, 1991)

$$\sigma\prime_{\mathrm{n}} = k_{\mathrm{n}} u_{\mathrm{n}}, \tag{3}$$

$$\tau = k_{\mathrm{s}} u_{\mathrm{s}}, \tag{4}$$

where k_{n} and k_{s} are the normal and shear stiffnesses of the fracture, respectively, $\sigma\prime_{\mathrm{n}}$ is the effective normal stress, τ is the shear stress projected onto the fracture plane, and u_{n} and u_{s} are normal and shear displacements along the fracture, respectively. A comparison of Eqs. (3) and (4) with the theory of linear elasticity for continuum material subject to uniaxial deformation conditions perpendicular to the fracture enables a rough estimate of the equivalent elastic moduli as functions of stiffness parameters (Yu et al., 2015; Zareidarmiyan et al., 2020)

$$E = k_{\mathrm{s}} \frac{(3k_{\mathrm{n}} - 4k_{\mathrm{s}})}{(k_{\mathrm{n}} - k_{\mathrm{s}})} s, \tag{5}$$

$$\nu = \frac{(k_{\mathrm{n}} - 2k_{\mathrm{s}})}{2(k_{\mathrm{n}} - k_{\mathrm{s}})}, \tag{6}$$

where E and ν are the equivalent Young's modulus and Poisson's ratio of the fracture, respectively. The normal and shear stiffness values for the fracture zones in this study are taken constant and, respectively, equal to 400 and 100 GPa/m, typical of a fractured granitic rock (Bandis et al., 1983; Min et al., 2004). Accordingly, Eqs. (5) and (6) yield Young's modulus of 6.67 GPa and Poisson's ratio of 0.33 for these fractures. We pick the elastic properties for the fault in a more straightforward manner. This large, mature fault has presumably undergone long-term slip, resulting in noticeable structural damage and proportionally low fault stiffness (Faulkner et al., 2006; Griffith et al., 2009). This stiffness contrast with the intact rock is taken into account by setting a very small Young's modulus of 1 GPa for the fault while using a Poisson's ratio identical to that of the reservoir (Table 1).

We analyze the evolution of fault and fracture stabilities using the Coulomb failure criterion. Accordingly, the Coulomb failure stress (CFS) is defined as

$$\mathrm{CFS} = \tau - \mu\sigma\prime_{\mathrm{n}}, \tag{7}$$

where μ is the friction coefficient. The increase in CFS, i.e., $\Delta\mathrm{CFS} > 0$, implies a reduction in stability until rupture occurs at $\mathrm{CFS} = 0$. The fault and fractures are assumed to be cohesionless in Eq. (7), resulting in a conservative stability assessment. We use a constant friction coefficient of 0.6, which is equivalent to a friction angle of 31° (Byerlee, 1978).

2.3 Numerical model description

We develop several numerical models to present a possible explanation for delayed earthquakes in EGS sites and explore the potential effects of post-injection protocols to manage them. The base-case model deals with an isolated fault geometry and consists in hydraulic stimulation for 250 h, followed by well shut-in, overall counting to a simulation period of 8000 h. We simulate water injection at a constant rate of 0.02 kg/s per cross-section area of the wellbore. The selected rate permits reproducing downhole pressure evolution representative of real-field practices. We run other simulations that consider well bleed-off after hydraulic stimulation while keeping all other parameters unchanged. To this end, a progressive reduction of pressure at the well is imposed until hydrostatic conditions are reached over a period of 24 h or 1 h and the hydrostatic pressure profile along the well is maintained afterward. These two scenarios are hereinafter referred to as slow and fast bleed-off, respectively. The numerical comparison between the two cases allows us to understand how the rate of depressurization could play a role in controlling post-injection seismicity. We repeat the simulations for another model setting where the fault is intersected by the fracture network with two injection periods of 84 or 200 h followed by either shut-in or fast bleed-off protocols, resulting in 4 distinct scenarios.

All simulations have identical initial and boundary conditions. Putting our focus on the hydromechanical response of the reservoir to hydraulic stimulation, the simulations are performed under a constant temperature of 90 °C. The reservoir is initially at hydrostatic pressure conditions. We consider a normal faulting stress regime, corresponding to extensional tectonic settings. The initial horizontal stress is assumed to be isotropic and given by $\sigma_{\mathrm{h}} = 0.58\sigma_{\mathrm{v}}$, in which σ_{v} is the overburden stress having a gradient of 25.9 MPa/km. Under this initial state of stress, the fault and fractures with a dip angle of 60° are critically stressed and, thus, small perturbations in stress and/or pressure are sufficient to destabilize them. We impose constant hydrostatic pressure at the top and no flow at the bottom and side boundaries as hydraulic boundary conditions. Mechanical boundary conditions include constant overburden stress at the top boundary and no displacements perpendicular to the other boundaries.

We numerically solve the hydromechanical problem described above using a fully-coupled finite element approach implemented in the software CODE_BRIGHT (Olivella et al., 1996). Simulations start with an initial equilibration phase to reach a steady-state in the pressure and stress fields across the domain. We use an unstructured mesh comprising nearly 29 000 first-order quadrilateral elements with refinement around regions of high pressure and deformation gradients, i.e., the injection well, the fault, and fractures (Fig. A1 in Appendix A). We use a constant element size of 2 m along the fault while decreasing it along the fractures from a maximum of 4 m down to 0.2 m toward fracture intersection and to 1 m toward the well. The thickness of the fault and fractures is discretized into a single element.

3 Results

3.1 Base-case simulation

3.1.1 Pore pressure changes in the fracture network

Water injection into the fracture network causes an increase in the pore pressure both in fractures and the

surrounding rock matrix (Fig. 2). The bottom-hole pore pressure change follows a sharp increase to nearly 18 MPa during injection for 24 h followed by a gentle, steady evolution to a maximum pressure of 23 MPa at the end of stimulation (Fig. 3). A similar trend is observed down along fracture f2, which is directly connected to the well. The observed decrease in the slope of the pore pressure changes can be attributed to the abrupt increase in fracture permeability (Fig. 1(c)), attenuating the pressure gradient along these flow conduits. Farther away from the wellbore and close to the limit of the fracture network (in fracture f5, point M_4 in Fig. 2(a)), the pore pressure increases linearly with time (Fig. 3), an evolution typical of a closed hydraulic system (Zhou et al., 2009). Indeed, fractures provide preferential flow pathways along which the pore pressure front propagates rapidly and reaches the boundaries of the fracture network. The pore pressure builds up to nearly 5 MPa at point M_4 (Fig. 3). Meanwhile, the overpressure diffuses only a few meters into the low-permeability matrix during the injection period (Fig. 2(a)).

After the injection stops, the overall hydraulic behavior of the fracture network is significantly affected by the post-stimulation protocols of shut-in or bleed-off. Following shut-in, the bottom hole pressure gradually declines as the overpressure generated during injection diffuses away from the well (Fig. 3). Pore pressure in a large body of the fracture network, e.g., in fractures f1, f2 and f4, follows a similar evolution to that of the well. In contrast, at larger distances from the well, e.g., at point M_4 close to the tip of fracture f5, the pore pressure continues to increase in the post-injection period, peaks at a value >6 MPa and declines afterward (Fig. 3). The fracture network maintains elevated pressures during the whole simulation time and keeps feeding a progressively growing pressurized region in the surrounding rock matrix (Fig. 2(d), (f)). In contrast, bleeding off the well reverses the flux toward the well and results in an abrupt bottom-hole pressure decline (Fig. 3). The depressurized fracture segments drain fluid out of the rock matrix, decreasing its pressure in the vicinity of the fractures but a persistent high-pressure zone remains away from the fractures due to the low permeability of the rock matrix (Fig. 2(b), (c), (e)). However, fractures become less responsive to bleed-off with distance from the well because they are not sufficiently permeable to effectively relax the overpressure in the large pressurized area within and around the fracture network. Similarly to the shut-in scenario, the pore pressure in the upper segment of fracture f5 continues to rise slightly in the post-injection period before a pressure decline takes place. The observed pore pressure evolution trends set a basis to explain hydromechanical processes underpinning the stability of the nearby fault as will be explained in the following.

3.1.2 Mechanisms of fault reactivation

Pore pressure buildup decreases the effective stress and expands the fractures and rock matrix to varying degrees. Fractures expand more perpendicular to their plane as they are less confined in this direction. The longitudinal expansion of the fractures is however constrained by the continuity of the displacement field across the interface with the surrounding matrix, which is stiffer and less pressurized and, thus, deforms to a smaller extent in the fracture direction. The larger the matrix stiffness and the pore pressure gradient perpendicular to the fractures, which entails a smaller extent of the pressurized matrix, the larger the constraints against longitudinal fracture expansion (De Simone et al., 2017). These deformation restrictions generate relatively large compressive stress parallel to the fracture planes (Fig. 4). The anisotropic change in the state of stress caused by the poroelastic effects gives rise to shear stress on the fracture planes. The shear stress build-up combined with the decrease in the effective normal stress could bring fractures to failure conditions and induce (micro) seismicity during the injection.

The coupled hydromechanical effects of water injection are not restricted to the fracture network. The injection-induced stress perturbations are instantaneously transmitted across the reservoir and resolve shear and normal stresses on the nearby fault plane (Fig. 4 and Fig. 5(c), (d) show the distribution of stress in the reservoir domain and along the fault, respectively). The compressive stress compacts and triggers an undrained hydromechanical response of the compliant fault during injection, leading to a pore pressure increase along the fault proportional to its Skempton coefficient (Skempton, 1954; Fig. 5(a)). The normal stress and, thus, the undrained pore pressure, continuously build up on the fault during injection as the pore pressure front penetrates the fractures with large opening components perpendicular to the nearby fault plane (Fig. 6(a)). In particular, the pore pressure increase at the tip of fracture f5 results in a spike in the normal stress and pressure in the middle of the fault toward the end of injection (Fig. 5(a)). The undrained compression causes an increase in the effective normal stress along the whole fault length (Fig. 5(c)), favoring its stability. Besides, the anisotropic stress changes generate shear stress, which is distributed non-uniformly along the fault depending on the relative location and orientation of fault segments to the fracture network. Under the normal faulting stress regime considered in this study, the shear stress increases on an upper fault segment and decreases on the remaining fault length during the injection (Fig. 5 (d)). The shear stress dominates the fault stability response to fluid injection as the CFS changes along the fault follows an overall similar trend (Fig. 5(e)): fault stability slightly decreases on the upper fault portion (positive ΔCFS) while increasing on the lower part (negative ΔCFS). However, the observed poroelastic stress perturbations are insufficient to reactivate the fault during injection.

After the injection stops, the pore pressure front diffuses from the tip of fracture f5 through the rock matrix and approaches the fault after a few hours. The pore pressure peaks in the middle of the fault shortly after stopping injection and then declines as it diffuses upward and downward along the fault (Fig. 6(a)). The pressurized rock between

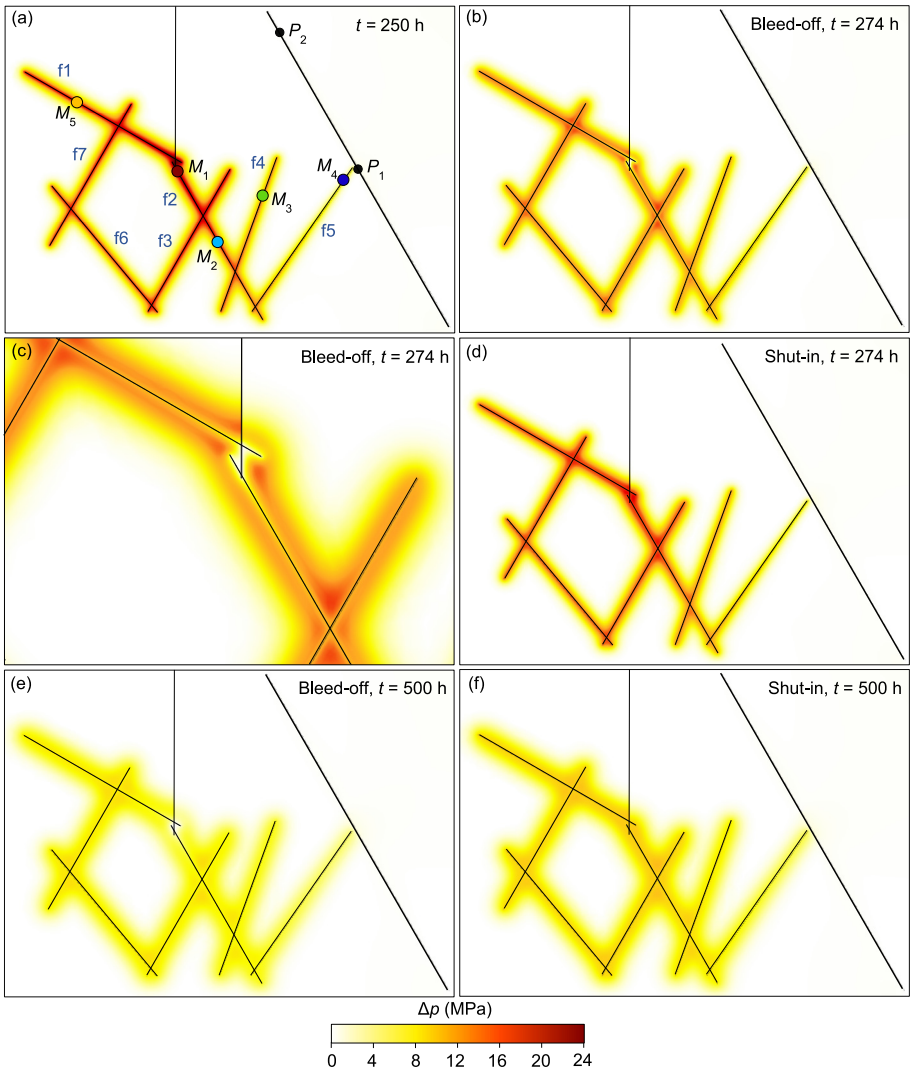

Fig. 2. Spatial distribution of pore pressure changes at several instants of time for shut-in and bleed-off: (a) after 250 h, i.e., at the end of injection, (b), (c) 24 h after the end of injection with a zoomed view of the fractures close to the wellbore in (c) for the scenario of fast well bleed-off, (d) 24 h after the end of injection with wellbore shut-in, and (e), (f) 250 h after the end of injection for scenarios of well bleed-off and shut-in, respectively.

the fracture and the fault acts as a point pressure source that drives a long-lasting diffusion of pore pressure. The pore pressure diffusion along the fault triggers a complex transient, coupled hydromechanical behavior, which is illustrated at different time intervals for a representative point on the upper fault patch in Fig. 6(b). Initially, the undrained pore pressure built up during the injection partially dissipates with time (interval I). Next, pore pressure diffusion creates a pressurized fault patch that dilates and transmits tensile stress ahead of the pressure front. As a result, each point along the fault first experiences dilation and, thus, pressure relief (interval II), then a pore pressure increase following the pressure front arrival (interval III) and finally a pressure decrease as the front moves away (interval IV). The pressure begins to build up along the whole fault length when the pressure front approaches the fault boundaries (interval V). The observed hydromechanical processes control the overall fault response in the post-injection period, appearing as a sequence of gradual increase in pore pressure (Fig. 5(a)), decrease in the effective normal stress (Fig. 5(c)), fault dilation and finally intrinsic permeability enhancement (Fig. 5(b)), which in turn promotes hydraulic diffusivity. Meanwhile, the shear stress undergoes minor changes (Fig. 5(d) and Fig. 6(a), (b)). The decrease in the effective normal stress degrades the frictional strength of the fault and, therefore, its stability with time (Fig. 6(e)). Stability changes are more pronounced along the upper fault segment, where the fault is already more critically stressed and prone to failure. The fault reactivates after more than 6 months potentially inducing a delayed earthquake.

3.1.3 Effect of bleed-off on fault reactivation

Results presented in Section 3.1.1 show that well bleed-off after stopping injection abruptly decreases the pore pressure at the bottom hole down along fracture f2 and some segments of the intersecting fractures while imposing minor, time-dependent changes in pore pressure farther

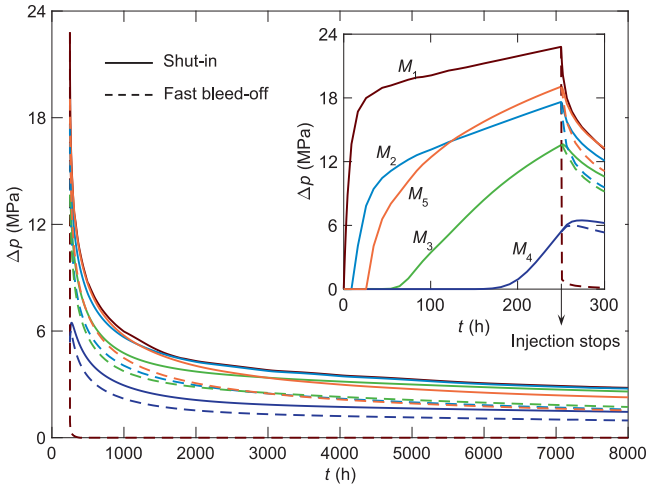

Fig. 3. Temporal evolution of injection-induced overpressure at five points (M_1 to M_5) in the fracture network for the two scenarios of well shut-in and fast bleed-off. The inset plot shows a zoom of pressure changes during and shortly after stopping injection. The locations of the points are illustrated in Fig. 2(a).

away from the well. The pore pressure attenuation reduces the compressive stresses along the fractures, in particular, the longitudinal stress built up during the injection, and suppresses fracture opening, which reduces the compressive stresses normal to fractures away from them. Therefore, bleed-off causes a rapid, anisotropic stress reduction that is transferred onto the nearby fault plane. On one hand, pressure relief along fracture f2 reduces the upward traction on the footwall of the upper fault segment, whose effect appears as a slight reduction in the shear stress on this fault segment compared to the case of shut-in (compare the dashed gray lines representing 24 h after stopping injection in Figs. 5(d) and 7(d) with reference to the solid blue line representing the end of injection). On the other hand, pressure reduction in fractures f3 to f5 relaxes the downward traction on the footwall of the lower portion of the fault and enhances the shear stress compared to the shut-in scenario (compare Fig. 7(d) with Fig. 5(d)). We also observe that shear stress changes with time are much larger on the lower fault segment compared to the upper fault segment. Yet, the lower fault segment remains far from slipping and the slight reduction in the shear stress at the upper, more critically stressed fault segment favors further fault stability (Fig. 7(e)).

Bleed-off drains the fracture network only partially but still affects the evolution of pore pressure along the fault in the post-injection period. Pore pressure reduction in the fracture network slightly attenuates the hydraulic connection with the fault and decreases pore pressure build-up in the middle of the fault (compare Fig. 6(c), (e) with Fig. 6(a)). The faster the bleed-off, the smaller the pressure buildup, although to a very small extent. A rapid bleed-off scenario, i.e., opening up the wellhead to achieve hydrostatic pressure conditions along the well over 1 h, gives rise to an overpressure in the middle of the fault smaller by approximately 0.15 MPa than that in the shut-in scenario (compare Fig. 7(a) with Fig. 5(a)). When bleeding off the well, the pressurized fault patch driven by hydraulic connection with the fracture network experiences a smaller reduction in the effective normal stress (compare Fig. 7(c) with Fig. 5(c)) and consequently, smaller increase in the intrinsic permeability (compare Fig. 7(b) with Fig. 5(b)). The extra overpressure in the shut-in scenario feeds a faster propagation of the pressure front downward, where the fault is less constrained by the applied stresses and flow takes place with further ease. While the pore pressure has already built up at the bottom end face of the fault at

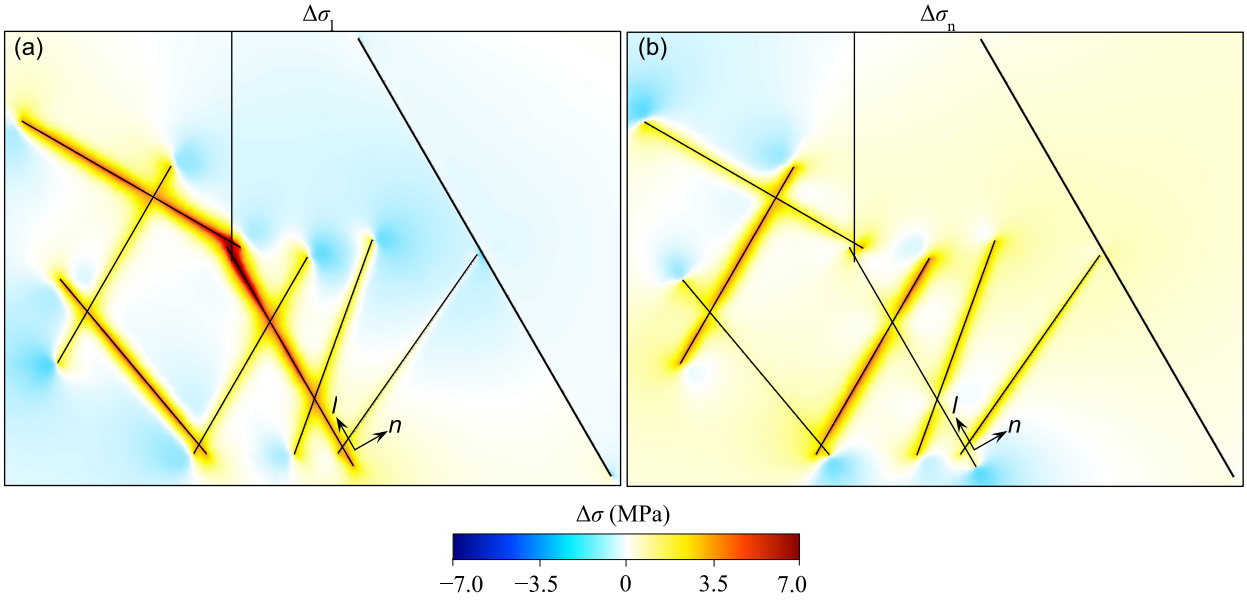

Fig. 4. Spatial distribution of (a) longitudinal stress in the direction of fracture f2 and (b) perpendicular stress to fracture f2 after 250 h, i.e., at the end of injection.

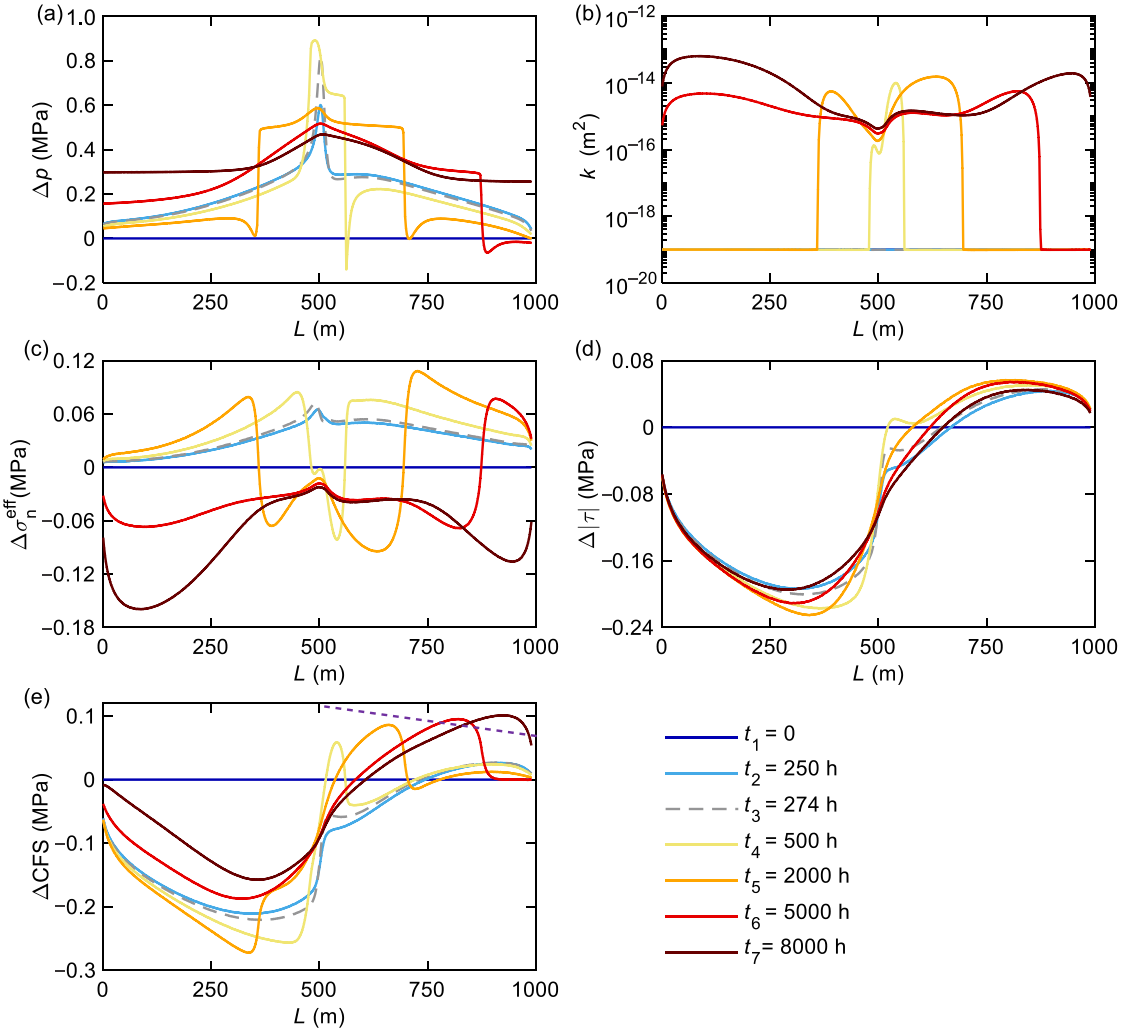

Fig. 5. Distributions of (a) pore pressure changes, (b) intrinsic permeability, (c) changes in the effective normal stress, (d) shear stress variations, and (e) evolution of fault stability in terms of CFS along the main fault at several times for the base-case model with well shut-in after stopping injection at $t = 250$ h. $L = 0$ m corresponds to the lower tip of the fault and increases upwards. The dashed purple line in (e) shows the required CFS change to cause slip along the fault.

$t = 5000$ h in the shut-in scenario (Fig. 5(a)), the pore pressure front lags more than 100 m behind in the case of rapid bleed-off (Fig. 7(a)). In contrast, bleed-off accelerates pore pressure diffusion upward along the fault. Indeed, the partial closure of fracture f2 as a result of bleed-off moderately relaxes the normal stress and the undrained pressure build-up on the upper fault segment (Fig. 7(a), (c)), opening up more readily when the pressure front approaches. Accordingly, the uppermost fault segment, e.g., point P_2, pressurizes several days to weeks earlier upon bleed-off (compare Fig. 6(d), (f) with Fig. 6(b)). The pressurized fault patch enlarges faster in the case of slow bleed-off as it corresponds to a higher fault pressure. The pore pressure increase on the upper fault segment consistently results in stability degradation ($\Delta CFS > 0$ in Fig. 7(e)), which is less pronounced compared to the case of shut-in due to smaller pressure build-up and slight shear stress reduction, but is large enough to initiate slip along the fault.

3.2 Case of fracture network intersecting the fault

We here present the results for the scenarios in which the fracture network intersects the fault and the stimulation lasts for either 84 or 200 h. Note that injection for 250 h, i.e., as long as the base-case scenario, would result in large fault pressurization and rupture soon after stopping the injection because the low-permeability matrix acting as a flow barrier between the fracture network and the fault does not exist anymore. After 84 h of injection, pore pressure hardly increases at the bottom of fracture f2 and a few meters along fracture f5 (Fig. 8(a)). The decreasing pore pressure in the fracture network in the post-injection period attenuates the undrained overpressure along the fault (see pressure drop after the stop of injection in Fig. 8(c)). Yet, pore pressure continues diffusing into fracture f5 and gradually builds up in the middle of the fault (point P_1 located 1 m below the fracture-fault intersection in Fig. 8

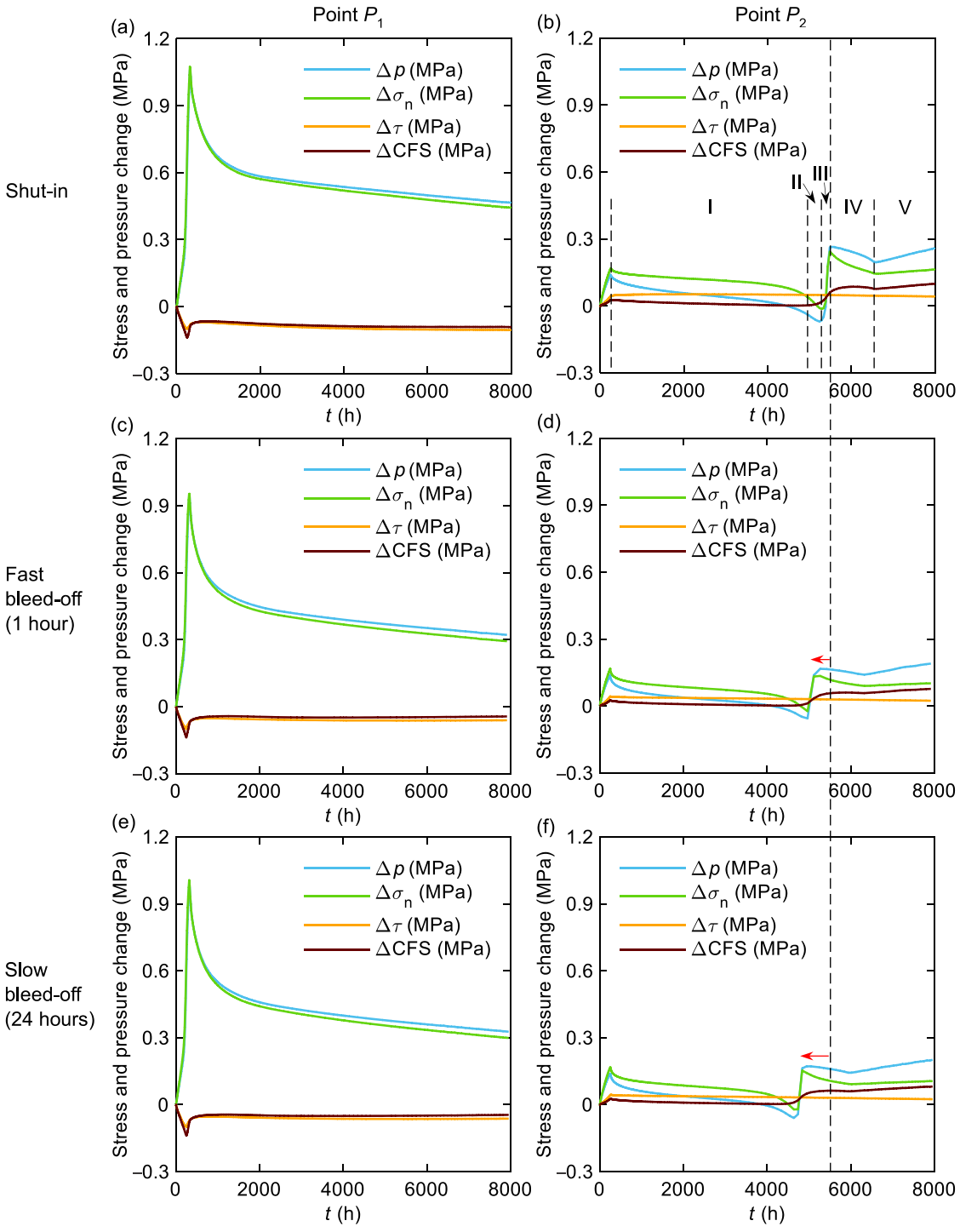

Fig. 6. Evolution with time of the changes in pore pressure, normal stress, shear stress and CFS at points P_1 and P_2 along the fault for (a), (b) the wellbore shut-in scenario, (c), (d) fast bleed-off scenario, and (e), (f) slow bleed-off scenario. The red arrows show the shift in time of the pore pressure front arrival at point P_2 caused by well bleed-off. The locations of the points P_1 and P_2 are illustrated in Fig. 2.

(c)). The growing longitudinal stress along fracture f5 projects normal stress onto the middle of the fault, preventing fault opening and flow along it. The pressure front begins to penetrate the fault as soon as the overpressure overcomes the normal stress at the intersection point with the fracture, whose effect appears as a rise in the slope of pore pressure evolution at point P_1 after 4000 h (Fig. 8(c)). Bleed-off speeds up pressure decline right after stopping injection while decreasing the rate of pressure increase afterward on the fault as it reverses flow in a large body of the fracture network. The pressure front advances very slowly along the fault and remains far from the boundaries during the 8000 h of simulation (point P_2 in Fig. 8(c)). The pressure increase in neither of the shut-in nor bleed-off scenarios would be eventually large enough to drive slip along the fault.

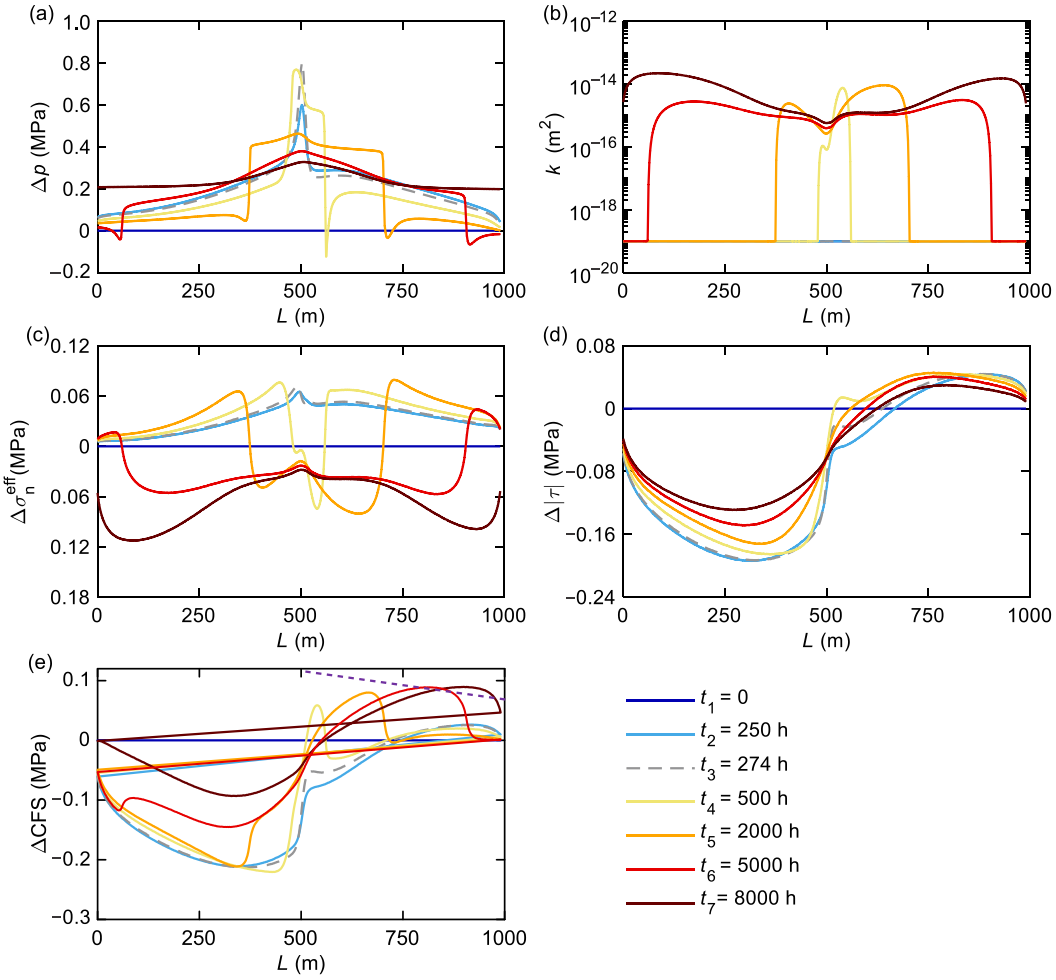

Fig. 7. Distributions of (a) pore pressure changes, (b) intrinsic permeability, (c) changes in the effective normal stress, (d) shear stress variations, and (e) evolution of fault stability in terms of CFS along the main fault at several times for the base-case scenario with slow well bleed-off after stopping injection at $t = 250$ h. $L = 0$ m corresponds to the lower tip of the fault and increases upwards. The dashed purple line in (e) shows the required CFS change to cause slip along the fault.

The pore pressure front obviously penetrates more into the fracture network and the surrounding rock matrix following a longer injection of 200 h (Fig. 8(b)). The overpressure peaks at nearly 1 MPa in the middle of the fault only a few hours after stopping the injection and drops abruptly afterward (Fig. 8(d)). The pressure decline in the middle fault segment takes place much faster than in the base-case scenario because flow toward the fault is established exclusively through fractures with low storage capacity, which entails rapid and large pressure changes following fault opening. Despite the direct hydraulic connection with the fracture network, the bleed-off effects on pore pressure and stress changes are similar to those explained above for the base-case scenario (Fig. 9). Pore pressure transmission from the fractures generates a persistent along-the-fault pressure front migration, promoted by fault opening and notable permeability enhancement (Fig. 9(a), (b)). Bleed-off even causes a faster upward pore pressure diffusion (note the earlier pressure increase at point P_2 in the case of bleed-off in Fig. 8(d)) as it contributes to relaxing the normal stress transmitted onto the fault plane during the injection (Fig. 9(c)). Yet, bleed-off slightly attenuates pore pressure build-up along the fault (Fig. 8) and further decreases shear stress on the upper fault portion in the post-injection period (Fig. 9(d)), both in favor of fault stability. The two effects counterbalance each other in a way that bleed-off overall imposes negligible influence on the fault reactivation behavior. Irrespective of the post-injection protocols, the pore pressure continuously redistributes to create an almost uniform profile along the whole fault length after a long period, e.g., $t = 14\ 000$ h (Fig. 9(a)). The resulting pore pressure increase of more than 0.2 MPa in the case of bleed-off and the corresponding reduction in the effective normal stress are large enough to eventually bring the fault to failure conditions (Fig. 9(e)). This result highlights that once a fracture network is pressurized, the propagation of pore pressure buildup farther from the well may not be prevented by bleeding off the well.

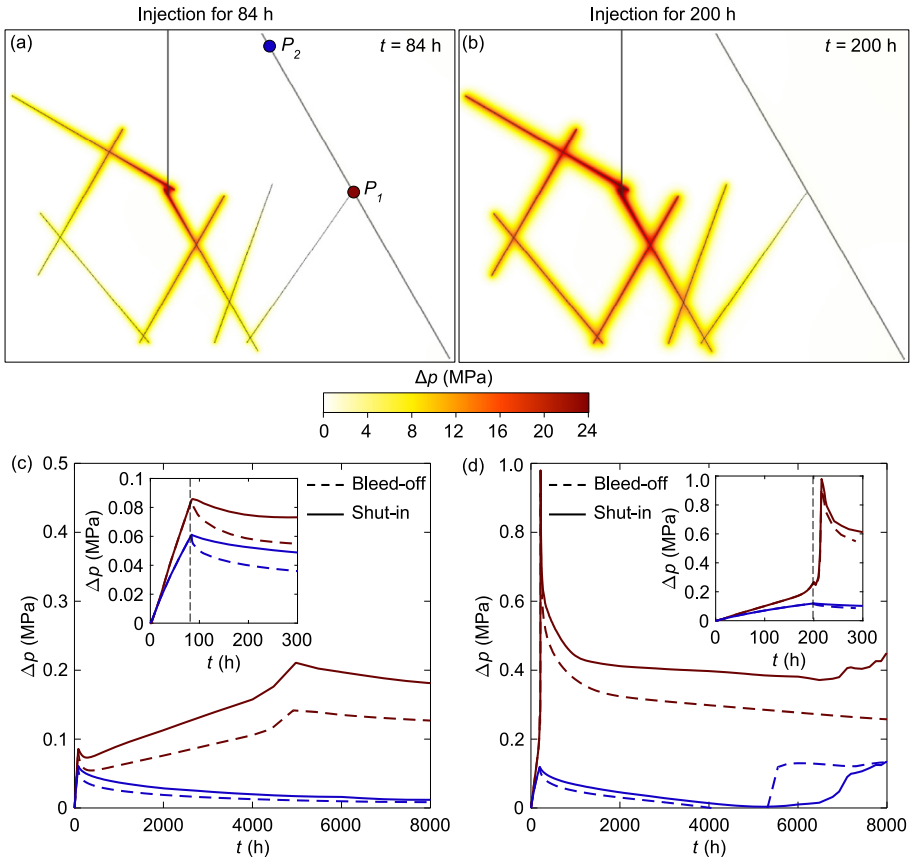

Fig. 8. Spatial distribution of overpressure at the end of (a) injection for 84 h and (b) injection for 200 h. Temporal evolution of pressure changes at points P_1 and P_2 along the fault (shown in (a) with the same colors as the corresponding curves) with shut-in and 1-h-long bleed-off post-injection scenarios for (c) 84 h and (d) 200 h of injection. The inset plots in (c), (d) show zooms of pressure changes during and shortly after stopping injection with the end of injection shown by vertical dashed black lines. Note that the pressure scales on the y axes of the plots are different.

4 Discussion

Simulation results propose a possible combination of mechanisms to explain delayed felt earthquakes induced by EGS projects: (1) poroelastic stressing as a result of uneven differential deformation of fractures under subsurface deformation constraints that instantaneously transmits non-negligible normal and shear stress on a large, nearby fault – some fault segments undergo an increase in shear stress and reduced stability while some others experience increase in normal stress and shear stress reduction which improves stability depending on their relative position and orientation to the fracture network, (2) undrained pore pressure build-up along the fault that partly offsets the stabilizing effect of the projected normal stress onto the fault plane, (3) long-lasting pore pressure transmission through stimulated fractures toward the fault, and (4) dilation-induced evolution of fault permeability that modulates the rate of pore pressure diffusion toward the critically-stressed fault segments (Fig. 10). The described sequence of mechanisms causes a time-dependent evolution of fault stability that eventually leads to fault rupture in the post-injection period and potentially induced seismicity if the fault is seismogenic.

Additional non-linearities in the hydromechanical response of the fracture network to fluid injection could be introduced by thermal stresses generated by the temperature difference between the injected fluid and the reservoir (Ghassemi & Zhou, 2011; De Simone et al., 2017; Kivi et al., 2022) and fracture slipping, either seismic or aseismic, driving static stress transfer to nearby fractures or faults (Wei et al., 2015; Vilarrasa et al., 2021; Kim et al., 2022; Ge & Saar, 2022). In particular, static stress transfer has been found to play a role in triggering post-injection earthquakes in multiple EGS sites (Cornet, 2016; Lengliné et al., 2017; Sáez and Lecampion, 2023; Boyet et al., 2023). However, induced events at these sites feature maximum time lags of a few days after stopping the injection. We have shown that delayed pore pressure migration could help explain induced earthquakes with time lags of several months, even longer than those observed at Pohang, South Korea (Kim et al., 2022) or at Cooper Basin (Jolokia-1), Australia (Baisch et al., 2015) EGS sites of nearly 2 and 4 months, respectively.

The gradual diffusion of pore pressure along the fault, which possesses the largest share in the observed delay in induced seismicity in this study, is affected by a transient coupled hydromechanical effect beyond the characteristic

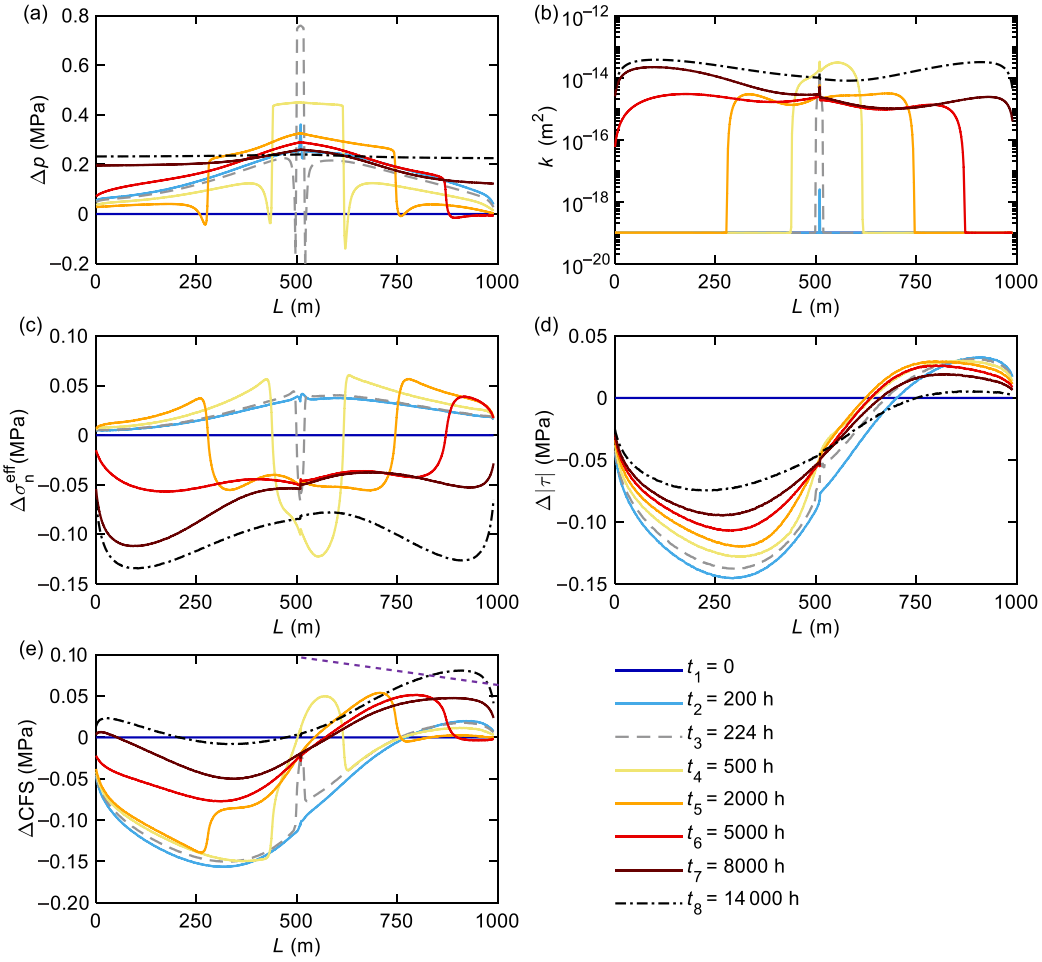

Fig. 9. Distributions of (a) pore pressure changes, (b) intrinsic permeability, (c) changes in the effective normal stress, (d) shear stress variations, and (e) evolution of fault stability in terms of CFS along the main fault at different times for the case of fault intersected by the fracture network with well bleed-off after stopping injection at $t = 200$ h. $L = 0$ m corresponds to the lower tip of the fault and increases upwards. The dashed purple line in (e) shows the required CFS change to cause slip along the fault.

length of pore pressure diffusion along the fault. Indeed, the fault opening outpaces fluid pressurization with the consequence of additional fault permeability enhancement and increased pressure gradient at the tip of the diffusing front, both promoting pressure migration (Vaezi et al., 2024). A similar phenomenon involving the propagation of both opening and slip displacement components has been demonstrated by in situ experiments at the Mont-Terri underground rock laboratory to offer an efficient driver of pore pressure transmission along low-permeability faults (Cappa et al., 2022).

Simulation results show that bleed-off gives rise to rapid depressurization in fractures in the vicinity of the injection wellbore, while imposing minor impacts on the far field (Fig. 10). The size of the fracture over which bleed-off effectively reverses flow and rapidly attenuates overpressure (named L^* here) is significantly limited and hardly exceeds half of the length of the fracture directly connected to the wellbore in the examined model setting, i.e., fracture f2 (Fig. 2). Nevertheless, our simulations could have slightly underestimated this characteristic length since they do not consider permanent permeability enhancement along the stimulated fractures by shearing-induced fracture dilation (Mallikamas & Rajaram, 2010; Vilarrasa et al., 2011; Rinaldi & Rutqvist, 2019). On the other hand, the size of the stimulated fracture network by pressure diffusion, L, taken as the length of the interconnected pathway through fractures from the wellbore, can be approximated by the square root of time, t, i.e., $L = \sqrt{4Dt}$, where D is the hydraulic diffusivity of the fractures (Talwani et al., 2007). Despite stopping injection, the stimulated reservoir volume continues to grow with time. If $L < L^*$, which is the case of short stimulations where the rupture is contained within or initiates from a stimulated fracture in the vicinity of the injection well, bleed-off could most likely prevent nucleation of an induced earthquake. In contrast, if $L \gg L^*$, corresponding to elongated injections and occasionally, but not necessarily, a rupture surface outside the stimulated reservoir volume, bleed-off becomes exceedingly ineffective in controlling post-injection seismicity. In particular, the low-permeability rock matrix surrounding the fracture network, if substantially pressurized, could persist in transmitting pore pressure to nearby faults. In this scenario, bleed-off could even accelerate rupture along a dis-

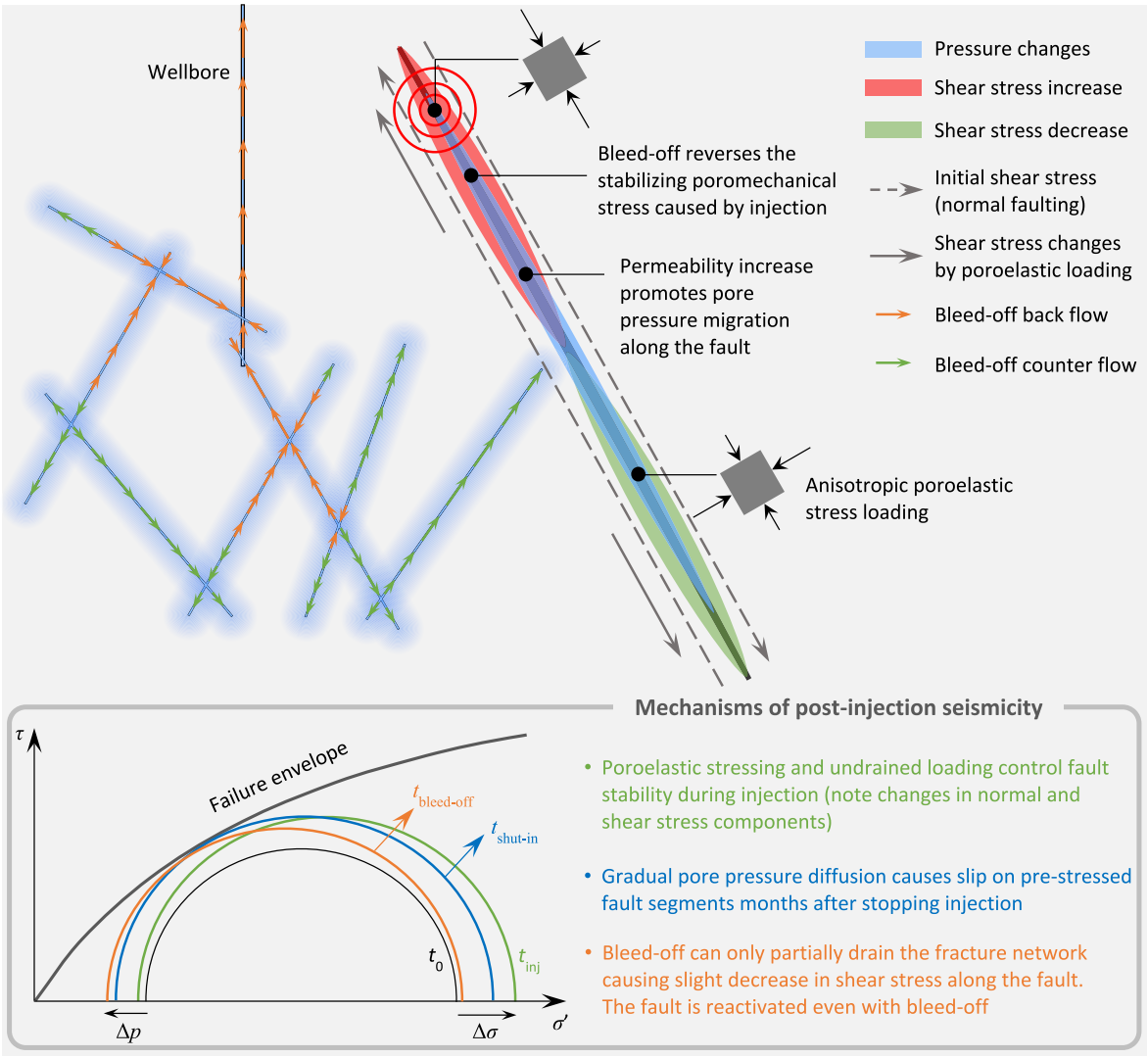

Fig. 10. Schematic summary of the processes contributing to post-stimulation seismicity in an EGS site.

tant fault surface by relaxing the poroelastic stabilizing stresses accumulated during injection, and even reversing the compressive stabilizing poroelastic stresses into tensile destabilizing ones, and promoting along-the-fault pressure diffusion (Fig. 10). The 2006 Basel, Switzerland, and the 2017 Pohang, South Korea, earthquakes provide examples of such events that continued and even exacerbated after bleed-off and are characterized by complex interactions between multiple structural features (Kim et al., 2022; Boyet et al., 2023). The two scenarios explained above, i.e., $L < L^*$ or $L \gg L^*$, are in agreement with the statistical analysis of the case histories of injection-induced seismicity by Shapiro et al. (2021), who found correlations between the occurrence probability and maximum magnitude of induced earthquakes with the time elapsed from the beginning of injection rather than the injected volume. Thus, the injection duration is a critical parameter in EGS project designs and requires optimization for the dynamics of the stimulated reservoir volume evolution to maintain controls on induced earthquakes.

This study highlights an EGS setting where bleed-off fails to effectively control post-stimulation seismic activities. Although the identified seismicity-triggering mechanisms could generally operate in different EGS settings, their contribution to fault reactivation and their spatiotemporal evolution in response to bleed-off depends largely on a variety of parameters, including (1) the relative position and orientation of the fault to stress distribution patterns formed around natural fractures, (2) fault stiffness, which controls deformation-induced pressure changes of the fault, and (3) stress-dependent hydraulic properties of the fault, which adjust flow along the fault (De Simone et al., 2017; Kivi et al., 2024a; Segall & Fitzgerald, 1998). Thus, the extension of some of the observed trends to other sites should be done carefully. A systematic understanding of under which conditions bleed-off could effectively control post-injection seismicity warrants complementary numerical simulations acknowledging involved coupled processes under different geological settings.

Insights gained from this study highlight the need for accurate site characterization and continuous monitoring

of the subsurface at different stages of developing an EGS project. A variety of characterization techniques should be employed to acquire detailed knowledge about subsurface structures and their multiphysical properties (Juanes et al., 2016; Kivi et al., 2023). Among others, field injection tests prior to the main stimulation phase could provide critical information about the hydromechanical properties of fractures intersecting the injection wellbore in addition to in situ stress conditions (Rutqvist & Stephansson, 1996; Vilarrasa et al., 2013; Park et al., 2020). Besides, physics-based models of the subsurface calibrated against field tests offer a powerful tool to identify and minimize the risk of injection-induced seismicity through fault stability analysis and appropriate design of the stimulation program, respectively (Rutqvist et al., 2015; Zang et al., 2019; Vilarrasa et al., 2021; Kivi et al., 2024b; Tangirala et al., 2024). These models should account for various earthquake-triggering mechanisms in combination with pore pressure diffusion. Additional subsurface structural and mechanistic complexities could be inferred from an integration of the models with a monitoring scheme that quantifies the evolution of reservoir response to fluid injection, mainly in terms of bottom-hole pressure and microseismicity. Such an integration, although challenging to achieve in (near) real-time (Tang et al., 2022), holds the promise of continuously characterizing the subsurface to reduce the subsurface uncertainties and improve seismicity prediction and management capabilities (Zhai et al., 2019; Vilarrasa et al., 2022). This study raises the necessity for subsurface monitoring after hydraulic stimulation for as long as several months during which pressure and stress perturbation continue to migrate away from the well, maintaining the risk of induced seismicity.

5 Conclusions

We find that a combination of multiple mechanisms could trigger post-stimulation earthquakes in EGS projects. Instantaneous poroelastic stress change could either increase or decrease stability on different segments of a nearby fault depending on their relative position and orientation to the stimulated fractures. Slight changes in pore pressure along critically-stressed fault patches, driven by time-dependent diffusion toward and along the fault, are enough to reactivate the fault. The considered model setting features delayed seismicity by several hours to months after stopping injection, spanning the range of field observations. Wellbore bleed-off after stopping injection slightly decreases shear stress and pore pressure buildup on the fault, favoring its stability. However, bleed-off may not ultimately prevent fault failure and may even accelerate it by relaxing normal stress on the fault, promoting pore pressure diffusion. Interestingly, only a limited portion of the fracture network in the vicinity of the wellbore remains responsive to bottomhole pressure changes and the depressurization signal attenuates rapidly beyond the area of influence. Thus, this behavior highlights a scenario where well bleed-off is not successful in controlling post-injection induced seismicity. We also conclude that the injection duration controlling the stimulated reservoir volume plays a key role in triggering seismicity and our ability to control it. Optimized injection and post-injection protocols should yet be explored in light of the involved coupled processes and subsurface structural features through proper monitoring and continuous characterization.

Data Availability

The input files and the FEM code CODE_BRIGHT used for numerical simulations in this study are publicly available at the institutional repository Digital. CSIC, which practices FAIR principles (https://doi.org/10.20350/digitalCSIC/16715).

CRediT authorship contribution statement

Iman R. Kivi: Writing – original draft, Visualization, Validation, Software, Resources, Methodology, Investigation, Funding acquisition, Formal analysis, Data curation, Conceptualization. **Victor Vilarrasa:** Writing – original draft, Validation, Supervision, Resources, Methodology, Funding acquisition, Formal analysis, Data curation, Conceptualization. **Kwang-Il Kim:** Writing – original draft, Validation, Methodology, Investigation, Funding acquisition, Formal analysis, Data curation. **Hwajung Yoo:** Writing – original draft, Validation, Methodology, Investigation, Formal analysis, Data curation. **Ki-Bok Min:** Writing – original draft, Validation, Supervision, Funding acquisition, Data curation, Conceptualization.

Declaration of competing interest

The authors declare that they have no known competing financial interests or personal relationships that could have appeared to influence the work reported in this paper.

Acknowledgment

I.R.K. and V.V. acknowledge support by the PCI2021-122077-2B project (www.easygeocarbon.com) funded by MCIN/AEI/10.13039/501100011033 and the European Union NextGenerationEU/PRTR. I.R.K. also acknowledges funding from the Engineering and Physical Sciences Research Council through the UKRI Postdoc Guarantee Award THMC4CCS [Grant No. EP/X026019/1]. V.V. also acknowledges funding from the European Research Council under the European Union's Horizon 2020 Research and Innovation Program through the Starting Grant GEoREST (www.georest.eu) under Grant agreement No. 801809. IMEDEA is an accredited "Maria de Maeztu Excellence Unit" (Grant CEX2021-001198, funded by MICIU/AEI/10.13039/501100011033). K.I.K. acknowledges support by the Innovative Technology Development Program for High-level waste management of the National

Research Foundation of Korea funded by the Korean government (Ministry of Science and ICT) (Grant No. 2021M2E3A2041312). K.-B.M. and H.Y. were supported by a grant from the Human Resources Development program (No. 20204010600250) of the Korea Institute of Energy Technology Evaluation and Planning, funded by the Ministry of Trade, Industry, and Energy of the Korean Government.

Appendix A Model grid

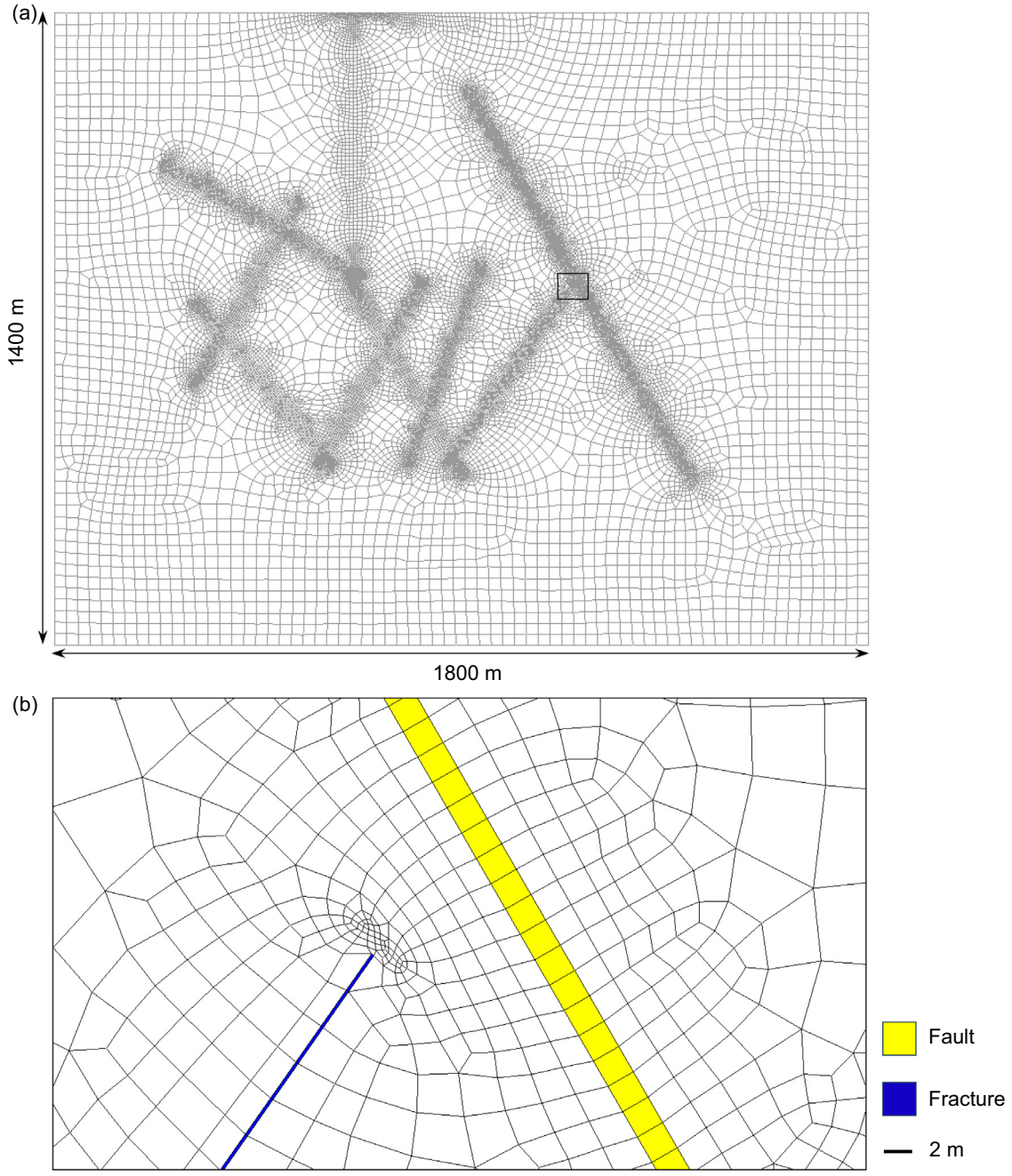

Fig. A1. (a) Finite element grid used in this study, and (b) a zoom of the mesh on part of the fault, the adjacent fracture and the surrounding rock matrix. The black box in (a) shows the location of the area used for plotting in (b). Model details and material layers can be found in Fig. 1.

References

Albaric, J., Oye, V., Langet, N., Hasting, M., Lecomte, I., Iranpour, K., ... Reid, P. (2014). Monitoring of induced seismicity during the first geothermal reservoir stimulation at Paralana, Australia. *Geothermics, 52*, 120–131.

Alghannam, M., & Juanes, R. (2020). Understanding rate effects in injection-induced earthquakes. *Nature Communications, 11*(1), 3053.

Bachmann, C. E., Wiemer, S., Woessner, J., & Hainzl, S. (2011). Statistical analysis of the induced Basel 2006 earthquake sequence: introducing a probability-based monitoring approach for Enhanced Geothermal Systems. *Geophysical Journal International, 186*(2), 793–807.

Baisch, S., Koch, C., & Muntendam-Bos, A. (2019). Traffic light systems: to what extent can induced seismicity be controlled?. *Seismological Research Letters 90*(3), 1145–1154.

Baisch, S., Rothert, E., Stang, H., Vörös, R., Koch, C., & McMahon, A. (2015). Continued geothermal reservoir stimulation experiments in the Cooper Basin (Australia). *Bulletin of the Seismological Society of America, 105*(1), 198–209.

Bandis, S. C., Lumsden, A. C., & Barton, N. R. (1983). Fundamentals of rock joint deformation. *International Journal of Rock Mechanics and Mining Sciences & Geomechanics Abstracts, 20*(6), 249–268.

Boyet, A., De Simone, S., Ge, S., & Vilarrasa, V. (2023). Poroelastic stress relaxation, slip stress transfer and friction weakening controlled post-injection seismicity at the Basel Enhanced Geothermal System. *Communications Earth & Environment, 4*(1), 104.

Buijze, L., van Bijsterveldt, L., Cremer, H., Paap, B., Veldkamp, H., Wassing, B. B., ... Jaarsma, B. (2019). Review of induced seismicity in geothermal systems worldwide and implications for geothermal systems in the Netherlands. *Netherlands Journal of Geosciences, 98*, e13.

Byerlee, J. (1978). Friction of rocks. In *Rock friction and earthquake prediction* (pp. 615–626). Basel: Birkhäuser Basel.

Cappa, F., Guglielmi, Y., Nussbaum, C., De Barros, L., & Birkholzer, J. (2022). Fluid migration in low-permeability faults driven by decoupling of fault slip and opening. *Nature Geoscience, 15*(9), 747–751.

Cornet, F. H. (2016). Seismic and aseismic motions generated by fluid injections. *Geomechanics for Energy and the Environment, 5*, 42–54.

De Simone, S., Carrera, J., & Vilarrasa, V. (2017). Superposition approach to understand triggering mechanisms of post-injection induced seismicity. *Geothermics, 70*, 85–97.

De Simone, S., Kivi, I. R., Min, K. B., & Rutqvist, J. (2023). Induced seismicity in EGS: observations and triggering mechanisms. In D. Chandrasekharam, & A. Baba (Eds.), *Enhanced Geothermal Systems (EGS)* (pp. 111–149). London: CRC Press.

Evans, K. F., Genter, A., & Sausse, J. (2005). Permeability creation and damage due to massive fluid injections into granite at 3.5 km at Soultz: 1. Borehole observations. *Journal of Geophysical Research: Solid Earth, 110*(B4).

Evans, K. F., Zappone, A., Kraft, T., Deichmann, N., & Moia, F. (2012). A survey of the induced seismic responses to fluid injection in geothermal and CO_2 reservoirs in Europe. *Geothermics, 41*, 30–54.

Faulkner, D. R., Mitchell, T. M., Healy, D., & Heap, M. J. (2006). Slip on'weak'faults by the rotation of regional stress in the fracture damage zone. *Nature, 444*(7121), 922–925.

Gaucher, E., Schoenball, M., Heidbach, O., Zang, A., Fokker, P. A., van Wees, J. D., & Kohl, T. (2015). Induced seismicity in geothermal reservoirs: A review of forecasting approaches. *Renewable and Sustainable Energy Reviews, 52*, 1473–1490.

Ge, S., & Saar, M. O. (2022). Induced seismicity during geoenergy development—a hydromechanical perspective. *Journal of Geophysical Research: Solid Earth, 127*(3), e2021JB023141.

Ghassemi, A., & Zhou, X. (2011). A three-dimensional thermo-poroelastic model for fracture response to injection/extraction in enhanced geothermal systems. *Geothermics, 40*(1), 39–49.

Goodman, R. E. (1991). *Introduction to rock mechanics* (2nd ed.). New York: John Wiley & Sons (Chapter 5).

Griffith, W. A., Sanz, P. F., & Pollard, D. D. (2009). Influence of outcrop scale fractures on the effective stiffness of fault damage zone rocks. *Pure and Applied Geophysics, 166*(10), 1595–1627.

Healy, J. H., Rubey, W. W., Griggs, D. T., & Raleigh, C. B. (1968). The denver earthquakes. *Science, 161*(3848), 1301–1310.

Hoseini, M., Bindiganavile, V., & Banthia, N. (2009). The effect of mechanical stress on permeability of concrete: a review. *Cement and Concrete Composites, 31*(4), 213–220.

Hsieh, P. A., & Bredehoeft, J. D. (1981). A reservoir analysis of the Denver earthquakes: a case of induced seismicity. *Journal of Geophysical Research: Solid Earth, 86*(B2), 903–920.

Ji, Y., Hofmann, H., Duan, K., & Zang, A. (2022). Laboratory experiments on fault behavior towards better understanding of injection-induced seismicity in geoenergy systems. *Earth-Science Reviews, 226*, 103916.

Jia, Y., Tsang, C. F., Hammar, A., & Niemi, A. (2022). Hydraulic stimulation strategies in enhanced geothermal systems (EGS): a review. *Geomechanics and Geophysics for Geo-Energy and Geo-Resources, 8*(6), 211.

Juanes, R., Jha, B., Hager, B. H., Shaw, J. H., Plesch, A., Astiz, L., ... Frohlich, C. (2016). Were the May 2012 Emilia-Romagna earthquakes induced? A coupled flow-geomechanics modeling assessment. *Geophysical Research Letters, 43*(13), 6891–6897.

Karvounis, D., & Wiemer, S. (2022). A discrete fracture hybrid model for forecasting diffusion-induced seismicity and power generation in enhanced geothermal systems. *Geophysical Journal International, 230*(1), 84–113.

Kim, K. I., Yoo, H., Park, S., Yim, J., Xie, L., Min, K. B., & Rutqvist, J. (2022). Induced and triggered seismicity by immediate stress transfer and delayed fluid migration in a fractured geothermal reservoir at Pohang, South Korea. *International Journal of Rock Mechanics and Mining Sciences, 153*, 105098.

Kivi, I. R., Boyet, A., Wu, H., Walter, L., Hanson-Hedgecock, S., Parisio, F., & Vilarrasa, V. (2023). Global physics-based database of injection-induced seismicity. *Earth System Science Data, 15*(7), 3163–3182.

Kivi, I. R., Pujades, E., Rutqvist, J., & Vilarrasa, V. (2022). Cooling-induced reactivation of distant faults during long-term geothermal energy production in hot sedimentary aquifers. *Scientific Reports, 12*(1), 2065.

Kivi, I. R., Vilarrasa, V., Kim, K. I., Yoo, H., & Min, K. B. (2024a). On the role of poroelastic stressing and pore pressure diffusion in discrete fracture and fault system in triggering post-injection seismicity in enhanced geothermal systems. *International Journal of Rock Mechanics and Mining Sciences, 175*, 105673.

Kivi, I. R., De Simone, S., & Krevor, S. (2024b). *An analytical tool for estimating fault slip probability for CO_2 storage resources under pressure constraints (No. EGU24-18221)*. Vienna, Austria: European Geosciences Union (EGU) General Assembly, https://doi.org/10.5194/egusphere-egu24-18221.

Kwon, S., Xie, L., Park, S., Kim, K. I., Min, K. B., Kim, K. Y., ... Lee, T. J. (2019). Characterization of 4.2-km-deep fractured granodiorite cores from Pohang Geothermal Reservoir, Korea. *Rock Mechanics and Rock Engineering, 52*(3), 771–782.

Lengliné, O., Boubacar, M., & Schmittbuhl, J. (2017). Seismicity related to the hydraulic stimulation of GRT1, Rittershoffen, France. *Geophysical Journal International, 208*(3), 1704–1715.

Majer, E. L., Baria, R., Stark, M., Oates, S., Bommer, J., Smith, B., & Asanuma, H. (2007). Induced seismicity associated with enhanced geothermal systems. *Geothermics, 36*(3), 185–222.

Mallikamas, W., & Rajaram, H. (2010). An improved two-dimensional depth-integrated flow equation for rough-walled fractures. *Water Resources Research, 46*(8), e2009wr008779.

McClure, M. W., & Horne, R. N. (2011). Investigation of injection-induced seismicity using a coupled fluid flow and rate/state friction model. *Geophysics, 76*(6), WC181–WC198.

McGarr, A. (2014). Maximum magnitude earthquakes induced by fluid injection. *Journal of Geophysical Research: Solid Earth, 119*(2), 1008–1019.

Min, K. B., Rutqvist, J., Tsang, C. F., & Jing, L. (2004). Stress-dependent permeability of fractured rock masses: a numerical study. *International Journal of Rock Mechanics and Mining Sciences, 41*(7), 1191–1210.

Mukuhira, Y., Dinske, C., Asanuma, H., Ito, T., & Häring, M. O. (2017). Pore pressure behavior at the shut-in phase and causality of large induced seismicity at Basel, Switzerland. *Journal of Geophysical Research: Solid Earth, 122*(1), 411–435.

Olivella, S., & Alonso, E. E. (2008). Gas flow through clay barriers. *Géotechnique, 58*(3), 157–176.

Olivella, S., Gens, A., Carrera, J., & Alonso, E. E. (1996). Numerical formulation for a simulator (CODE_BRIGHT) for the coupled analysis of saline media. *Engineering Computations, 13*(7), 87–112.

Park, S., Kim, K. I., Xie, L., Yoo, H., Min, K. B., Kim, M., ... Meier, P. (2020). Observations and analyses of the first two hydraulic stimula-

tions in the Pohang geothermal development site, South Korea. *Geothermics, 88*, 101905.
Rinaldi, A. P., & Rutqvist, J. (2019). Joint opening or hydroshearing? Analyzing a fracture zone stimulation at Fenton Hill. *Geothermics, 77*, 83–98.
Rutqvist, J. (2012). Fractured rock stress–permeability relationships from in situ data and effects of temperature and chemical–mechanical couplings. In T. Gleeson, & S. E. Ingebritse (Eds.), *Crustal permeability* (pp. 65–82). John Wiley & Sons.
Rutqvist, J., & Stephansson, O. (1996). A cyclic hydraulic jacking test to determine the in situ stress normal to a fracture. *International Journal of Rock Mechanics and Mining Sciences & Geomechanics Abstracts, 33* (7), 695–711.
Rutqvist, J., Dobson, P. F., Garcia, J., Hartline, C., Jeanne, P., Oldenburg, C. M., ... Walters, M. (2015). The northwest Geysers EGS demonstration project, California: pre-stimulation modeling and interpretation of the stimulation. *Mathematical Geosciences, 47*(1), 3–29.
Sáez, A., & Lecampion, B. (2023). Post-injection aseismic slip as a mechanism for the delayed triggering of seismicity. *Proceedings of the Royal Society A, 479*(2273), 20220810.
Schmittbuhl, J., Lambotte, S., Lengliné, O., Grunberg, M., Jund, H., Vergne, J., ... Masson, F. (2021). Induced and triggered seismicity below the city of Strasbourg, France from November 2019 to January 2021. Comptes Rendus. *Géoscience, 353*(S1), 561–584.
Schultz, R., Ellsworth, W. L., & Beroza, G. C. (2022). Statistical bounds on how induced seismicity stops. *Scientific Reports, 12*(1), 1184.
Segall, P., & Fitzgerald, S. D. (1998). A note on induced stress changes in hydrocarbon and geothermal reservoirs. *Tectonophysics, 289*(1–3), 117–128.
Segall, P., & Lu, S. (2015). Injection-induced seismicity: poroelastic and earthquake nucleation effects. *Journal of Geophysical Research: Solid Earth, 120*(7), 5082–5103.
Shapiro, S. A., Audigane, P., & Royer, J. J. (1999). Large-scale in situ permeability tensor of rocks from induced microseismicity. *Geophysical Journal International, 137*(1), 207–213.
Shapiro, S. A., Kim, K. H., & Ree, J. H. (2021). Magnitude and nucleation time of the 2017 Pohang Earthquake point to its predictable artificial triggering. *Nature Communications, 12*(1), 6397.
Skempton, A. W. (1954). Coherent-potential model of substitutional alloys. *Géotechnique, 4*, 143–147.
Talwani, P., Chen, L., & Gahalaut, K. (2007). Seismogenic permeability, ks. *Journal of Geophysical Research: Solid Earth, 112*, B07309.
Tang, M., Ju, X., & Durlofsky, L. J. (2022). Deep-learning-based coupled flow-geomechanics surrogate model for CO_2 sequestration. *International Journal of Greenhouse Gas Control, 118*, 103692.
Tangirala, S. K., Parisio, F., Vaezi, I., & Vilarrasa, V. (2024). Effectiveness of injection protocols for hydraulic stimulation in enhanced geothermal systems. *Geothermics, 120*, 103018.
Taron, J., Elsworth, D., & Min, K. B. (2009). Numerical simulation of thermal-hydrologic-mechanical-chemical processes in deformable, fractured porous media. *International Journal of Rock Mechanics and Mining Sciences, 46*(5), 842–854.
Tomac, I., & Sauter, M. (2018). A review on challenges in the assessment of geomechanical rock performance for deep geothermal reservoir development. *Renewable and Sustainable Energy Reviews, 82*, 3972–3980.
Vaezi, I., Alcolea, A., Meier, P., Parisio, F., Carrera, J., & Vilarrasa, V. (2024). Numerical modeling of hydraulic stimulation of fractured crystalline rock at the bedretto underground laboratory for geosciences and geoenergies. *International Journal of Rock Mechanics and Mining Sciences, 176*, 105689.
Verdon, J. P., & Bommer, J. J. (2021). Green, yellow, red, or out of the blue? An assessment of Traffic Light Schemes to mitigate the impact of hydraulic fracturing-induced seismicity. *Journal of Seismology, 25*(1), 301–326.
Vilarrasa, V., Carrera, J., & Olivella, S. (2013). Hydromechanical characterization of CO_2 injection sites. *International Journal of Greenhouse Gas Control, 19*, 665–677.
Vilarrasa, V., De Simone, S., Carrera, J., & Villaseñor, A. (2021). Unraveling the causes of the seismicity induced by underground gas storage at Castor, Spain. *Geophysical Research Letters, 48*(7), e2020GL092038.
Vilarrasa, V., De Simone, S., Carrera, J., & Villaseñor, A. (2022). Multiple induced seismicity mechanisms at Castor underground gas storage illustrate the need for thorough monitoring. *Nature Communications, 13*(1), 3447.
Vilarrasa, V., Koyama, T., Neretnieks, I., & Jing, L. (2011). Shear-induced flow channels in a single rock fracture and their effect on solute transport. *Transport in Porous Media, 87*(2), 503–523.
Wei, S., Avouac, J. P., Hudnut, K. W., Donnellan, A., Parker, J. W., Graves, R. W., ... Eneva, M. (2015). The 2012 Brawley swarm triggered by injection-induced aseismic slip. *Earth and Planetary Science Letters, 422*, 115–125.
Wibberley, C. A., & Shimamoto, T. (2003). Internal structure and permeability of major strike-slip fault zones: the Median Tectonic Line in Mie Prefecture, Southwest Japan. *Journal of Structural Geology, 25* (1), 59–78.
Witherspoon, P. A., Wang, J. S., Iwai, K., & Gale, J. E. (1980). Validity of cubic law for fluid flow in a deformable rock fracture. *Water Resources Research, 16*(6), 1016–1024.
Yu, Y., Damians, I. P., & Bathurst, R. J. (2015). Influence of choice of FLAC and PLAXIS interface models on reinforced soil–structure interactions. *Computers and Geotechnics, 65*, 164–174.
Zang, A., Oye, V., Jousset, P., Deichmann, N., Gritto, R., McGarr, A., ... Bruhn, D. (2014). Analysis of induced seismicity in geothermal reservoirs–an overview. *Geothermics, 52*, 6–21.
Zang, A., Zimmermann, G., Hofmann, H., Stephansson, O., Min, K. B., & Kim, K. Y. (2019). How to reduce fluid-injection-induced seismicity. *Rock Mechanics and Rock Engineering, 52*(2), 475–493.
Zareidarmiyan, A., Salarirad, H., Vilarrasa, V., Kim, K. I., Lee, J., & Min, K. B. (2020). Comparison of numerical codes for coupled thermo-hydro-mechanical simulations of fractured media. *Journal of Rock Mechanics and Geotechnical Engineering, 12*(4), 850–865.
Zhai, G., Shirzaei, M., Manga, M., & Chen, X. (2019). Pore-pressure diffusion, enhanced by poroelastic stresses, controls induced seismicity in Oklahoma. *Proceedings of the National Academy of Sciences, 116* (33), 16228–16233.
Zhou, Q., Birkholzer, J. T., & Tsang, C. F. (2009). A semi-analytical solution for large-scale injection-induced pressure perturbation and leakage in a laterally bounded aquifer–aquitard system. *Transport in Porous Media, 78*(1), 127–148.